PROCEEDINGS A

royalsocietypublishing.org/journal/rspa

Research

Cite this article: Pang Y, Sun W, Liu T. 2024 Quasi-static responses of marine mussel plaques detached from deformable wet substrates under directional tensions. *Proc. R. Soc. A* **480**: 20230465.
https://doi.org/10.1098/rspa.2023.0465

Received: 3 July 2023
Accepted: 16 April 2024

Subject Areas:
materials science, mechanical engineering, biomechanics

Keywords:
Mytilus edulis, mussel plaque, surface traction, digital image correlation, optical microscope

Author for correspondence:
Tao Liu
e-mail: tao.liu@qmul.ac.uk

Electronic supplementary material is available online at https://doi.org/10.6084/m9.figshare.c.7204009.

THE ROYAL SOCIETY PUBLISHING

Quasi-static responses of marine mussel plaques detached from deformable wet substrates under directional tensions

Yong Pang[1], Wei Sun[2] and Tao Liu[1]

[1]School of Engineering and Materials Science, Queen Mary University of London, London E1 4NS, UK
[2]Faculty of Engineering, University of Nottingham, Nottingham NG7 2RD, UK

YP, 0000-0002-9205-5003; TL, 0000-0003-2713-3674

Quantifying the response of marine mussel plaque attachment to wet surfaces remains a significant challenge to a mechanistic understanding of plaque adhesion. Here, we develop a novel, customized microscope system, combined with two-dimensional *in situ* digital image correlation (DIC), to quantify the in-plane deformation of a deformable substrate that interacts with a mussel plaque under directional tension. By examining the strain field within the substrate, we acquired an understanding of the mechanism by which in-plane traction forces are transmitted from the mussel plaque to the underlying substrate. Finite-element (FE) models were developed to assist in the interpretation of the experimental measurement. Our study revealed a synergistic effect of pulling angle and substrate stiffness on plaque detachment, with mussel plaques anchoring to a 'stiff' substrate at small pulling angles, i.e. natural anchoring angles, having mechanical advantages with higher load-bearing capacity and less plaque deformation. We identify two distinct failure modes, i.e. shear-traction-governed failure (STGF) and normal-traction-governed failure (NTGF). It was found that increasing the stiffness of the substrate or reducing the pulling angle results in a change of the failure mode from NTGF to STGF. Our findings offer new insights into the mechanistic understanding of mussel plaque–substrate interaction, providing a plaque-inspired strategy to develop high-performance and artificial wet adhesion.

1. Introduction

Underwater adhesion is a common phenomenon in aquatic organisms, allowing them to survive in harsh natural environments [1–4]. It can be achieved through different mechanisms that operate on the macro- or micro-/nano-scale, including suction [5–7], capillarity [8–12], interlocking [13–18] and protein-based chemical bonds. The adhesive mechanism that involves chemical bonds, particularly in marine mussels, has recently received considerable attention [19–22]. The thread–plaque system of marine mussels represents a remarkable design in nature. This system serves to anchor marine mussels to diverse wet surfaces, including salt-encrusted and corroded rock surfaces (figure 1*a*) that are relatively stiff [23,24], as well as the skin of marine organisms that are relatively soft [25]. A radially distributed thread–plaque system can provide a strong anchorage up to 10 times the self-weight of mussels (figure 1*b*), enabling mussels to survive the hydrodynamic forces exerted by tidal currents or the force of predators hoping to dislodge them for a meal.

In addition to the interaction of protein-based chemistry at adhesion sites [22,26,27], recent research progress has indicated that the unique adhesive structure of a mussel plaque plays a crucial role in achieving strong wet adhesion [28–30]. A typical adhesive structure of a mussel plaque consists of an outer, dense protective cuticle layer [31,32], collagen fibre bundles [33] and a low-density, porous plaque core [29,34], as shown in figure 1*c*. The plaque core exhibits a porous structure consisting of a disordered, foamy network of pores at length scales ranging from the nanoscale (90–120 nm) to the microscale (1.5–2.5 µm) (figure 1*f*), which is reminiscent of cellular solids [35–37] or truss lattices [38–43]. The cuticle layer is approximately 4 µm in thickness (figure 1*g*), and is covered by granules at the length scale of 0.5 µm (figure 1*d*). Granule hydrations preserve moisture and flexibility for the cuticle layer, maintaining high energy absorption under external loads during low tide [44]. The cuticle layer and the plaque core work cooperatively to achieve strong load-bearing capacity under dynamic [30,45] and static loads [45,46].

Our scanning electron microscope (SEM) investigation has revealed a distinct pore densification near the interface between the plaque core and the underlying substrate (figure 1*e*,*f*), which has not yet been reported in previous studies [29,34,47]. The presence of this pore arrangement may be related to the load distribution at the interface between the plaque and the underlying substrate. Understanding the deformation patterns of deformable substrates can offer fundamental insight into how traction forces are transmitted from mussel plaque to the underlying substrate, as well as the failure mechanisms at the adhesive interface.

To strengthen the understanding of mussel plaque detachment, the following research gaps identified in recent studies need to be addressed. Previous research has identified factors that affect plaque detachment, including pulling angles [30,48], substrate surface conditions [49–51], strain rates [52] and loading cycles [52–54] through experimental studies. However, these experimental studies were carried out primarily in moist or dry environments [30,48,53], which could not fully capture the responses and failure mechanisms of plaque detachment that occur underwater. In addition, studies on the mechanosensing mechanism of mussel feet found that mussels prefer stiff or hydrophilic surfaces for anchoring [50,55]. However, the mechanical benefits of anchoring to these substrates remain unclear. Furthermore, inspired by the porous core of marine mussels, a semi-analytical approach combined with finite-element (FE) simulation has been successfully applied to study the effects of pore arrangement on detachment behaviour [56]. It was found that void size, gradation or volume fraction can be used to manipulate maximum pulling force, elongation at failure and energy dissipation of detachment. However, the full-field deformation imposed on the substrate by the porous structure needs further investigation.

To date, no experimental evidence has been reported on traction force distributions at mussel plaque–substrate interfaces. The direct measurement of the traction forces at interfaces with rigid substrates still presents a significant challenge. Nonetheless, measuring the deformation

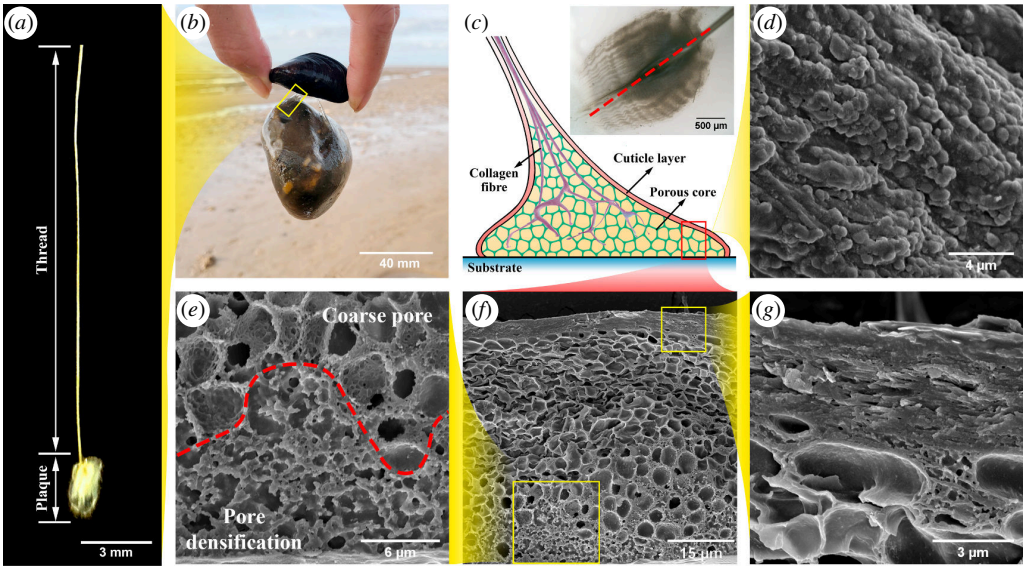

Figure 1. The unique adhesive structure of a mussel plaque. (*a*) A plaque–thread system of a marine mussel (from a blue mussel). (*b*) The plaque–thread systems are capable of supporting a rock weighing 248 g, which is approximately 6–10 times heavier than the mussel itself. (*c*) Schematic of the cross-section of a mussel plaque showing the internal structure, with the inset showing the top view of a real mussel plaque and the dashed line showing the direction of the section. (*d*) Micrograph of distal thread surface covered by protective granular composite structure. (*e*) Micrograph showing pore densification in the vicinity of plaque and substrate interface. (*f*) Overview of the hierarchical adhesive microstructure of mussel plaque. (*g*) The cross-section shows the thickness of the cuticle layer, approximately 4 µm.

pattern on a flexible substrate can offer insights into how traction forces are transmitted from a plaque to the underlying surface. This article aims to achieve three objectives: first, we develop a novel microscope platform, incorporating high-resolution *in situ* digital image correlation (DIC), to measure the deformation of flexible substrates. Second, full-scale FE models are developed and validated by DIC measurements to provide interpretation for the quasi-static responses at plaque–substrate interaction. Third, we explore the failure mechanisms at the plaque–substrate interface, which reveals the mechanical advantages of anchoring to 'stiff' substrates at a smaller pulling angle in nature.

2. Methods

(a) Mussel sample preparation

Blue mussels (*Mytilus edulis*) were collected from the Hunstanton mussel farm (52.94°N, 0.49°E) in England (electronic supplementary material, figure S1*a* [57]) and kept in an insulated cooler with natural seawater (temperature = 7°C, salinity = 33 ppt) during the shipment. Before placing mussel samples in to the aquarium, the salinity tester was calibrated with a standard 35 ppt calibration sachet, and then the salinity and temperature of artificial seawater were checked by a Hanna HI-98319 tester. These mussels were further placed in a laboratory aquarium (600 × 1200 × 600 mm) filled with continuously circulated seawater (electronic supplementary material, figure S1*b* [57]). Sea salt (Tropic Marin Pro-Reef Sea Salt, UK) was dissolved in fresh water to simulate natural seawater conditions (salinity = 33 ppt and pH = 8). The pH of artificial seawater was measured by pH test strips (Simplex Health™). An aquarium chiller was used to maintain seawater temperatures ranging from 5 to 7°C, and an aeration system was used to

supply adequate oxygen to the artificial seawater. A daily partial water change was implemented, replacing 10% of the total water volume to maintain water quality. Shellfish Diet 1800 (Reed Mariculture, USA), a mixture of marine microalgaes, was used to feed the mussels daily. To eliminate the variation between plaques, mussel samples of identical size were fastened with substrates (electronic supplementary material, figure S1*c* [57]) to allow plaque deposition for 48 h. The plaque–thread systems of mussels used for the SEM analysis and mechanical tests were carefully cut from the same mussel.

(b SEM

To prepare cryo-sections for SEM imaging, polydimethylsiloxane (PDMS) substrates with deposited plaques were carefully peeled from polymethyl methacrylate (PMMA) base (electronic supplementary material, figure S1*d* [57]), and then fixed in a solution of 3.7% formaldehyde and 2.5% glutaraldehyde for approximately 4 h. Subsequently, they were placed in Milli-Q water for 3 days at 0–5°C. These samples were quickly frozen in the embedding medium (Thermo Scientific OCT) at −40°C using Leica cryostat (CM3050S) and then sliced into thick cryosections (40 µm) at a cryochamber temperature of −20°C to prevent them from curling and warping during subsequent sample drying. Cryo-sections were further rinsed three times in Milli-Q water to remove the cryoprotectant. An incremental solvent exchange method was used from Milli-Q water to ethanol to hexamethyldisilazane (HMDS) to prevent samples from rapidly becoming stiff and brittle during the freeze-drying process [29,58,59]. The mass ratio of ethanol in water/ethanol exchange was altered from 0 to 100% in increments of 25%, and then the mass ratio of HMDS in ethanol/HMDS exchange underwent an increase from 0 to 100% in increments of 33%. Finally, SEM samples were sputter coated with 10 nm thick iridium layers for 2 min and imaged in JEOL 7000 SEM using an accelerating voltage of 5 kV.

(c) Substrate fabrication

PDMS was used to fabricate transparent substrates that allow plaque-imposed deformation measurable with the aid of microparticles. Dow Corning Sylgard 184 silicone elastomer (10:1 wt.% for base and curing agent) and Sylgard 527 silicone gel (1:1 wt.% for parts A and B) were mixed with different mass ratios to tune Young's modulus from 0.57 ± 0.01 to 1.68 ± 0.05 (electronic supplementary material, table S1 [57]). The mechanical properties of different PDMS formulations (electronic supplementary material, figure S2*b–e* [57]) were characterized using standard tensile specimens according to ASTM D412 [60] (electronic supplementary material, figure S2*a* [57]). Once the stiffness of different PDMS formulations was determined, four-layer substrates (figure 2*a*) were built layer upon layer using spin coating with different combinations of spin speed and duration (electronic supplementary material, table S2 [57]). PMMA plates with a dimension of $60 \times 60 \times 2$ mm were used as the base for the PDMS coating. The PDMS layers were coated twice to achieve a thickness of approximately 200 µm. This thickness ensures that the mechanical property of PDMS is thickness independent (electronic supplementary material, figure S2*f* [57]), and the substrate deformation is measurable and comparable [61]. Microparticles were mixed with PDMS to create a monolayer of randomly distributed particles for deformation tracking. Black liquid silicone pigment (Easycomposites, UK) was added into the fourth layer of the PDMS at a mass ratio of 1%, which reduces the reflective lights from the plaque and enhances the imaging contrast of microparticles. Both the particle layer and the pigment layer were spin coated with an ultra-thin thickness of approximately 15 µm using the same PDMS formulation as the PDMS layer. This thickness approached the manufacturing limits of the spin coating (Laurell WS-650-23B).

To investigate the effects of substrate stiffness on plaque detachment, PDMS is an ideal candidate material that can tune the stiffness while maintaining a consistent roughness

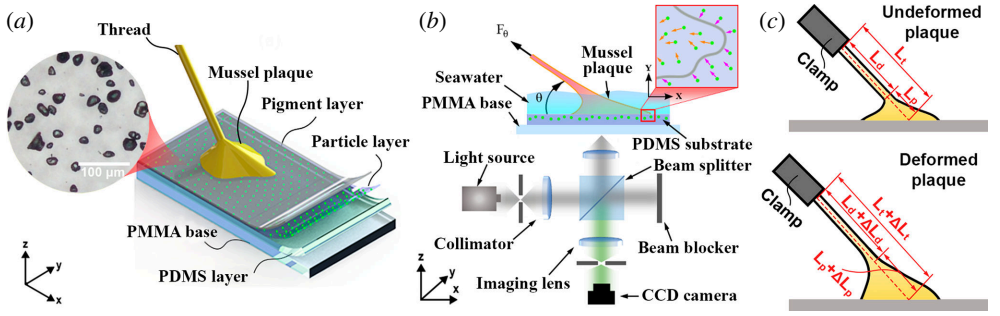

Figure 2. Experimental approaches for the characterization of plaque/substrate interaction. (*a*) Fabrication of four-layer PDMS substrates for mussel plaque deposition. (*b*) The schematic of the customized microscope system used in the directional tensile tests. (*c*) The schematic of a mussel thread–plaque system in undeformed and deformed states.

and hydrophilicity. Since surface hydrophilicity and roughness play a significant role in wet adhesion [62], these factors were assessed by water contact angle (WCA) and atomic force microscope (AFM), respectively. Representative WCAs and surface topographies show insignificant differences between different PDMS substrates (electronic supplementary material, figure S3*c* and *d* [57]). Thus, it can be confirmed that plaque detachment behaviours are not affected by surface hydrophilicity and roughness.

(d) Mechanical tests

A customized microscope system was designed to characterize the surface tractions of plaque attachment, failure modes of plaque detachment (figure 2*b* and electronic supplementary material, figure S4*a* and *b* [57]) and deformations of substrates. To measure the mechanical responses under wet conditions, the test samples were fully immersed in seawater during the experiment, as shown schematically in figure 2*b*. Directional tensile loads, with respect to the substrate from 15 to 90° at increments of 15°, were applied to the mussel threads via a linear actuator (Thomson MLA11A05), at a loading speed of 50 µm/s. This loading speed was sufficiently slow to measure the quasi-static responses of the plaque–thread systems as the measured responses were not sensitive to further reduction of the loading speed. A high-resolution load cell (Honeywell Model 34 with a precision of 0.01 N) was attached between the rigid clamp and linear actuator to measure the load response during the tests. Displacement and force data were recorded by a custom-written program using an Arduino Nano board. Randomly distributed microparticles provided a strong reflection under the illumination of a LED light (Edmund Optics, 530 nm). The 12 × zoom imaging systems equipped with two CCD cameras (Pixelink PL-D USB 3.0 CMOS) were used to capture deformations of plaques and substrates. In the tests, the CCD camera was configured to match the loading speed at a frame rate of 50 fps .

Throughout the article, the global coordinates x, y, z are defined as follows: the x-axis is aligned with the projection of the thread on the substrate; the z-axis is perpendicular to the substrate, and the y-axis is determined by the right-hand rule. Under a directional tensile load $\mathbf{F}_\theta(\mathbf{F}_\theta = F_\theta\mathbf{n})$, the average surface traction ($\mathbf{T}$) and its shear (T_t) and normal (T_n) components can be defined as

$$\mathbf{T} = \frac{F_\theta}{A}\mathbf{n} = T_t\boldsymbol{e_x} + T_n\boldsymbol{e_z}, \tag{2.1}$$

$$T_t = \frac{1}{A}\int_A t_t dA = \frac{F_\theta \mathrm{Cos}\theta}{A}, \tag{2.2}$$

$$T_n = \frac{1}{A}\int_A t_n dA = \frac{F_\theta \mathrm{Sin}\theta}{A}, \tag{2.3}$$

where $\mathbf{n}$ and F_θ denote the direction vector and magnitude of the tensile force applied to the free end of the mussel thread (figure 2*b*), respectively; $\boldsymbol{e_x}$ and $\boldsymbol{e_z}$ are the unit vectors in the x- and z-directions, respectively; t_t and t_n are the normal (z-direction) and tangential (x-direction) components of the local surface traction, respectively; θ is the pulling angle defined as an angle from the projection of the thread on the substrate to the thread in the clockwise direction (figure 2*b*); A is the area of the projection of a mussel plaque on the underlying substrate, defined as the area enclosed by the red dashed curve in figure 3*e*. The total tensile strain of a thread–plaque system $\boldsymbol{\varepsilon_t}(\boldsymbol{\varepsilon_t} = \varepsilon_t\mathbf{n})$, the strain of the plaque in the system $\boldsymbol{\varepsilon_p}(\boldsymbol{\varepsilon_p} = \varepsilon_p\mathbf{n})$ and the strain of the thread in the system $\boldsymbol{\varepsilon_d}(\boldsymbol{\varepsilon_d} = \varepsilon_d\mathbf{n})$ can be defined as

$$\varepsilon_t = \frac{\Delta L_t}{L_t} = \frac{\Delta L_d + \Delta L_p}{L_d + L_p}, \tag{2.4}$$

$$\varepsilon_p = \frac{\Delta L_p}{L_p}, \tag{2.5}$$

$$\varepsilon_d = \frac{\Delta L_d}{L_d}, \tag{2.6}$$

where L_t, L_d and L_p represent the original lengths of thread–plaque system, the thread and the plaque under undeformed configuration, respectively (figure 2*c*), with $L_t = L_d + L_p$. Deltas ΔL_d and ΔL_p denote the elongations of the thread and the plaque, respectively. In the tests, the total elongation ΔL_t was measured directly from the linear actuator, ΔL_d was measured optically from the CCD camera (electronic supplementary material, figure S4*b* [57]) and ΔL_p was determined by $\Delta L_p = \Delta L_t - \Delta L_d$. Since plaque–thread systems vary in initial geometries that may cause considerable variation in ΔL_t, tensile strains determined by equations (2.4)–(2.6) allow the deformation comparable in different plaque–thread systems.

(e) Two-dimensional *in situ* DIC

Two-dimensional *in situ* DIC measurement was implemented in DICe software [63], and microparticles (ZnS:Cu) [64,65], as tracking features for full-field displacement measurements, were randomly distributed in PDMS (electronic supplementary material, figure S3*a* [57]). Other microparticles can also be applied to DIC measurement as long as they meet imaging criteria of high image contrast, high particle randomness, suitable particle size (3–5 pixels) and particle density (25–50%) [66–68]. The particle size followed a normal distribution in all substrates, and the radius of the particle (mean ± s.d.) was between 10.26 ± 5.32 µm and 10.80 ± 5.36 µm (electronic supplementary material, figure S3*b* [57]). The microparticle pattern was imaged using the microscope system at a spatial resolution of 362 pixels/mm, resulting in a minimum resolvable displacement and principal strain of 3 µ and 0.001, respectively. The region of interest in DIC measurement was 600 × 600 pixels, and the step size was configured as 32 pixels. The subset image was set as 32 × 32 pixels to include approximately 6–9 particles, which ensures the optimal particle density of approximately 25–50% for the DIC measurement [69–72].

(f) FE simulations

Full-scale, three-dimensional FE simulations were conducted using the commercially available FE solver ABAQUS/Explicit. Each FE model contained five components, a thread, a cuticle layer, a plaque core, a cohesive interface and a substrate, as shown in figure 3*c,f*. Directional

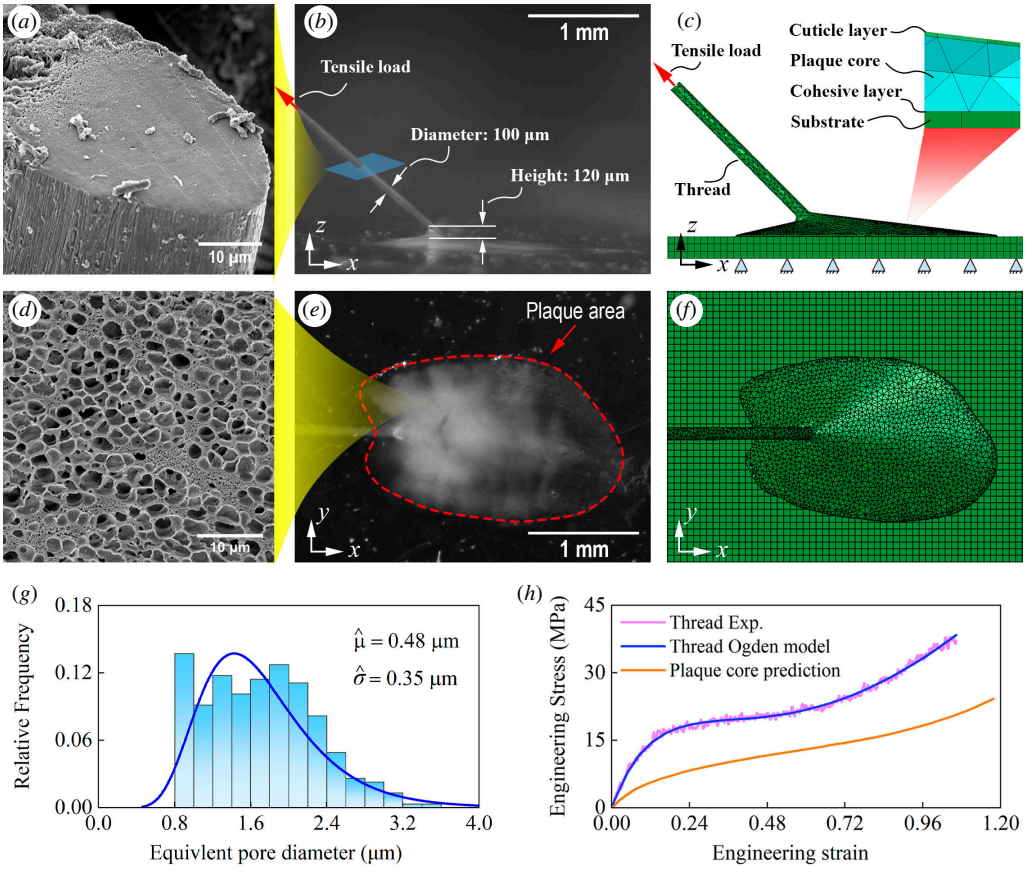

Figure 3. The FE model for the plaque–thread system. (*a*) The cross-section of mussel thread. (*b*) and (*c*) The side view of a real plaque–thread system and FE model, respectively. (*d*) Porous microstructures in mussel plaque core. (*e*) The projection of a real mussel plaque on a substrate. (*f*) Top view of the FE model. (*g*) Pore size distribution of mussel plaque core. (*h*) Determination of thread and plaque core properties for FE simulation.

tensile loads were applied to the end of the mussel thread using displacement control, as shown in figure 3*b*,*c*. The dimensions of the FE models were chosen in accordance with those of the real mussel plaques (e.g. figure 3*b*,*e*): the thread is approximately 100 µm in diameter; the mussel plaque, a core-shell structure, covered by a 4 µm thick cuticle layer (as measured in figure 1*g*), is 120 µm in height. The thread and plaque core were modelled with 4-node three-dimensional tetrahedral elements, i.e. the C3D4 elements in ABAQUS notation, and the cuticle layer was modelled with 6-node three-dimensional wedge elements (C3D6 elements). Quantifying the complete tensile stress–strain relationship of the cuticle layer from experiments is inherently challenging owing to two main reasons: separating the cuticle layer from the porous core and conducting micro-level tensile tests on the cuticle layer in wet conditions. Therefore, the reasonable assumption should be made to simulate the mechanical behaviour of the plaque–thread system. The SEM images suggest that both the thread and the cuticle layer possess a similarly dense, solid microstructure (figures 3*a* and 1*g*). They were assumed to have similar mechanical behaviour and were, therefore, modelled using an identical material model. A uniaxial tensile test was conducted to determine the mechanical behaviour of a single thread, in which the strain was defined by equation (2.6). The experimental result of a single thread tension was fitted into the three-term Ogden model [73]

$$\Psi(\bar{\lambda}_1, \bar{\lambda}_2, \bar{\lambda}_3) = \sum_{k=1}^{N} \frac{2\mu_k}{\alpha_k^2}(\bar{\lambda}_1^{\alpha_k} + \bar{\lambda}_2^{\alpha_k} + \bar{\lambda}_3^{\alpha_k} - 3), \tag{2.7}$$

where $\bar{\lambda}_k$ are distortional principal stretches which can be calculated from principal stretches (λ_k) by $\bar{\lambda}_k = J^{-1/3}\lambda_k$, N is the order of the strain energy potential ($N = 3$), k is the index of summation ($k = 1, 2, 3$), J is the elastic volume strain, $J = \lambda_1\lambda_2\lambda_3$ and μ_k and α_k are the material constants. As shown in figure 3*h*, the mechanical response of the mussel thread can be captured by Ogden's model using the material data listed in table 1.

The plaque cores exhibit porous structures with porosity in the range 37.4–60.2% [29,34,74]. The mechanical property of the plaque cores was estimated based on the FE simulations on the two-dimensional representative volume element (RVE) under the uniaxial tension with periodic boundary conditions [75]. The RVE was created by mimicking the pore distribution within the plaque cores using the approach described by [76]. SEM images such as figure 3*d* were used to measure the pore distributions. To consider pore variations between and within the plaques, SEM images were obtained from three distinct mussel plaques (electronic supplementary material, figure S10 [57]) and three slices of a single mussel plaque (electronic supplementary material, figure S11 [57]). By taking the average of these six SEM images, the pores in the mussel plaque achieved the best fit using a log-normal distribution with a mean of the logarithmic value of the radius ($\hat{\mu}$) of 0.48 µm and a s.d. of the logarithmic value of the radius ($\hat{\delta}$) of 0.35 µm (figure 3*g*). The parent material of the RVE was assumed to be identical to that of the cuticle layer. Figure 3*h* shows the predicted mechanical behaviour which is fitted by Ogden's model (equation (2.7)) using the material data listed in table 1. Numerical tests suggested that the predictions obtained by three-dimensional RVEs did not show significant differences from those obtained by two-dimensional RVEs.

The PDMS substrate, with dimensions of $3.2 \times 2.7 \times 0.2$ mm, was modelled with 8-node three-dimensional brick elements with a reduced integration scheme (C3D8R elements). Both the numerical and experimental measurements suggested that the tensile loads were insufficient to trigger nonlinear substrate responses. Therefore, the substrates were modelled as linear elastic materials using a Young's modulus of $E = 1.68$ MPa for stiff PDMS and $E = 0.56$ MPa for 'soft' PDMS (electronic supplementary material, figures S2*b*,*e* [57]) and a Poisson's ratio of 0.49 [77].

The mussel foot proteins (mfps) between the plaque and the substrate, an ultra-thin adhesive layer of less than 15 nm [78], were modelled with 6-node three-dimensional cohesive elements (COH3D6 elements). Let t_n and t_s denote the z-direction normal and y-direction tangential components of the local surface traction, respectively, and δ_n, δ_t and δ_s are the normal and shear separations corresponding to tractions. The adhesive behaviour of mfps was defined by the following traction versus separation relation [79]

$$t_n = \begin{cases} (1-D)k_n\delta_n, & \text{for } \delta_n > 0 \\ k_n\delta_n, & \text{otherwise} \end{cases}, \tag{2.8}$$

$$t_s = (1-D)k_s\delta_s, \tag{2.9}$$

$$t_t = (1-D)k_t\delta_t, \tag{2.10}$$

where k_n, k_s and k_t are the normal and shear stiffness, respectively, and the damage variable $D \in [0, 1]$ has the initial value of 0. For compression, i.e. $\delta_n \leq 0$, the damage variable does not affect the cohesive relation. The onset of damage was assumed when the following quadratic interaction criterion reached a value of unity

$$\left\{\frac{t_n}{t_n^o}\right\}^2 + \left\{\frac{t_s}{t_s^o}\right\}^2 + \left\{\frac{t_t}{t_t^o}\right\}^2 = 1, \tag{2.11}$$

Table 1. Material properties of plaque/substrate system used in FE simulation.

materials	material constants used for FE simulation						
		μ_1(MPa)	α_1	μ_2(MPa)	α_2	μ_3(MPa)	α_3
thread and cuticle layer		−134.25	1.29	19.84	2.77	181.07	−3.93
plaque core		−17.08	5.99	8.62	6.64	33.69	−8.21
cohesive layer properties on:	t_n^o (MPa)	t_s^o(MPa)	t_t^o (MPa)	K_n (MPa/mm)	K_s (MPa/mm)	K_t (MPa/mm)	G_c (J/m^2)
stiff PDMS	0.38	0.30	0.30	13 000	1200	1200	102
soft PDMS	0.16	0.25	0.25	12 000	1100	1100	102
	Young's modulus, E (MPa)				Poisson's ratio, υ		
stiff PDMS substrate	1.68				0.49		
soft PDMS substrate	0.56				0.49		

where t_n^o, t_s^o and t_t^o denote the maximum traction when the separation is either purely normal or pure shear, respectively. To define the damage evolution of the cohesive layer, a linear softening law based on fracture energy was used. We define an effective separation by

$$\delta_e = \sqrt{\langle \delta_n \rangle^2 + \delta_s^2 + \delta_t^2}\,. \tag{2.12}$$

The work conjugated effective traction to this effective separation can be defined as

$$t_e = \sqrt{\langle t_n \rangle^2 + t_s^2 + t_t^2}\,. \tag{2.13}$$

The damage variable D is then defined in terms of the fracture energy G_c as

$$D = \frac{\frac{2G_c}{t_e^o}(\delta_e^{\max} - \delta_e^o)}{\delta_e^{\max}(\frac{2G_c}{t_e^o} - \delta_e^o)} \leq 1, \tag{2.14}$$

where $\delta_e^{\max}$ is the maximum value of δ_e attained during the loading history while t_e^0 and δ_e^0 are the values of effective traction at the initiation of damage.

The material parameters that define the interface model are the maximum tractions t_n^o, t_s^o and t_t^o; the stiffnesses k_n, k_s and k_t; and fracture energy G_c. It was found that soft substrate weakens mussel wet adhesion through mechanosensing [50,55,80]. Therefore, two sets of interface properties were used to simulate plaques anchoring to the stiff and the soft PDMS substrates, respectively, as listed in table 1. The maximum tractions (t_n^o, t_s^o and t_t^o) and the stiffnesses (k_n, k_s and k_t) were estimated by calibrating the FE predicted traction T—total strain ε_t responses against their experimental results (figure 4*a*,*b*).

Numerical experiments were conducted to ensure that the outcomes of the numerical simulations were independent of the mesh density in the FE simulations. Thus, the thread, cuticle layer, plaque core, cohesive interface and substrate for each FE model were meshed using global sizing control with an approximate global mesh size of 50 µm. To ensure the simulations captured the quasi-static responses of the system, the loading rate was controlled to ensure that the kinetic energy of the system was within 5% of the total energy.

3. Results

(a) Responses of a thread–plaque system under directional tensions

In a natural environment, the mussel thread–plaque system and the underlying substrate often maintain an angle of < 45° [22,81]; however, the pulling angles may exceed this range (i.e. θ = 0–90°) under the conditions of strong tidal waves. Therefore, directional tensions were conducted at the pulling angles selected from 0 to 90° to examine the mechanical behaviours of the plaque detachment. In the tests, the thread of all samples was cut in a unified length of approximately 6 mm, which is approximately 50 times larger than the plaque height of 120 µm. This thread length to plaque height ratio ensured that the measured mechanical responses could represent the detachment behaviour of a real mussel thread–plaque system. Figure 4*a*,*b* shows the representative traction T − total strain ε_t responses of mussel plaque detached from stiff and soft PDMS substrates, respectively. For both cases, the value of ε_t at failure decreases as the pulling angle increases. At a smaller pulling angle (e.g. θ = 15°), the mechanical response of a plaque attachment can be characterized by four regimes: linear elastic, plateau, hardening and failure. However, as the pulling angle increases, a plaque may fail before reaching the hardening regime.

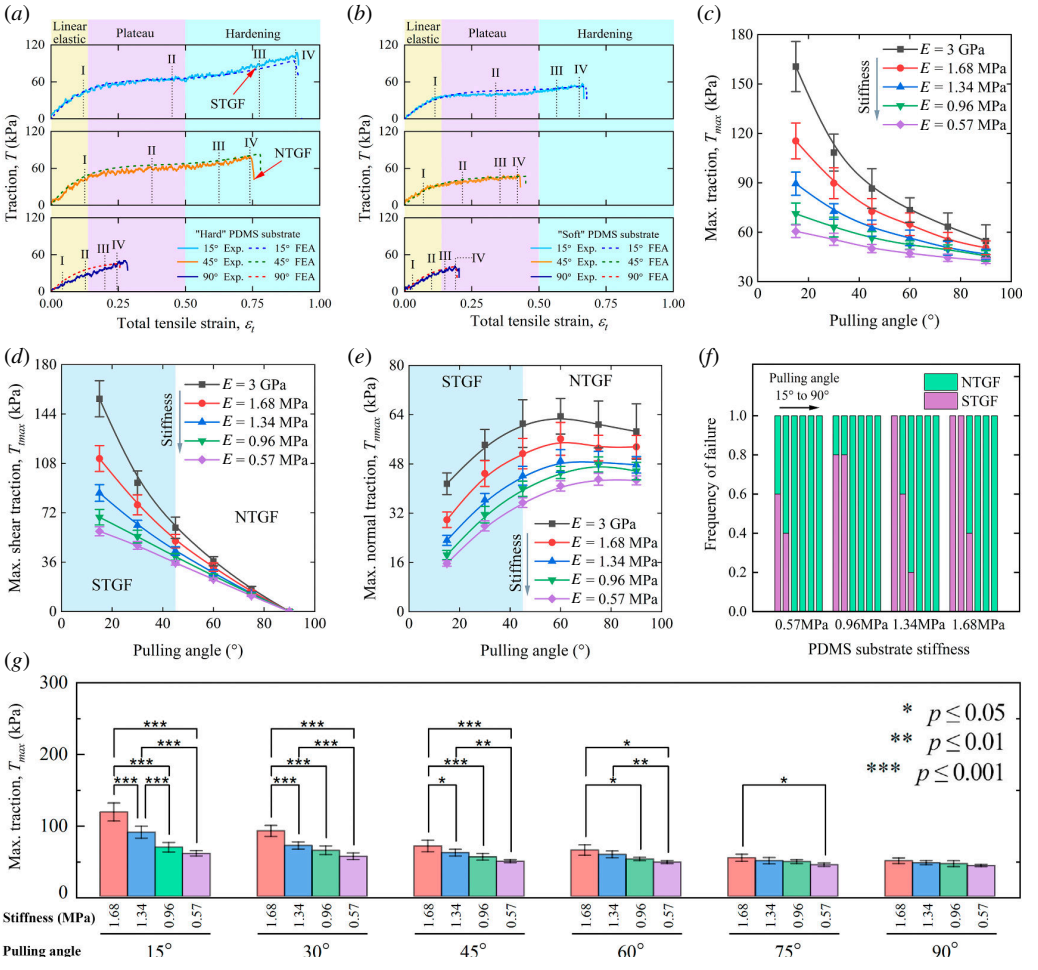

Figure 4. Mechanical responses of a mussel thread–plaque system under directional tension. (*a*) and (*b*) Representative surface traction (T)—total strain (ε_t) curves of plaque detachment from stiff and soft PDMS substrates, respectively. (*c*)–(*e*) The average maximum traction (T_{max}), shear (T_{smax}) and normal traction (T_{nmax}) as a function of pulling angle, respectively. (*f*) The frequency of STGF and NTGF) in response to different combinations of pulling angle and substrate stiffness. (*g*) Statistical analysis for substrate stiffness and pulling angles. *P*-values < 0.05 were considered statistically significant (*$P \leq 0.05$, **$P \leq 0.01$ and ***$P \leq 0.001$). Note: the data are means ± s.d. ($n = 5$ for each pulling angle) and individual surface traction (T)—total strain (ε_t) curves are given in electronic supplementary material, figures S5–S9 [57].

To investigate the effects of substrate stiffness and pulling angle on mechanical responses, the average maximum traction $T_{max} = \max\{T\}$ as a function of the pulling angle θ was plotted in figure 4*c*. It was found that T_{max} decreases with an increase in the pulling angle for a given substrate stiffness. This finding was reminiscent of peeling behaviours of adhesive films or hydrogels in previous studies, which investigated the effects of pulling angles on the peeling force [82–84]. Consistent with the observations of existing research [48], under the identical substrate stiffness condition, the value of T_{max} decreases as the pulling angle increases; the stiffness of the substrate has a significant effect on the value of T_{max} at a smaller pulling angle, say $\theta = 15^\circ$, i.e. the value of T_{max} increases with the stiffness of the substrate. However, the effect of substrate stiffness diminishes as the pulling angle increases; the effect of substrate stiffness becomes insignificant at $\theta = 90^\circ$. To examine the failure mechanisms, the maximum shear and normal components, $T_{tmax} = max\{T_t\}$ and $T_{nmax} = max\{T_n\}$, of the surface traction **T** as a function of the pulling angle θ are shown in figure 4*d*,*e*, respectively. The maximum shear component

T_{tmax} is sensitive to the pulling angle; the values at $\theta \geq 45^{\circ}$ are < 50% of that at $\theta = 15^{\circ}$. As the plaque detachment was primarily caused by the normal component T_n at $\theta = 90^{\circ}$, one can estimate the strength of the adhesion under normal surface traction based on the response at $\theta = 90^{\circ}$ (figure 4*e*). In contrast, the maximum normal traction T_{nmax} is less sensitive to the pulling angle; the values at $\theta \geq 45^{\circ}$ remain approximately similar to the adhesion strength. These results suggest that (i) plaques fail in NTGF mode when the pulling angles are greater than 45°, whereas they are more prone to fail in the STGF mode when pulling angles are less than 45°; (ii) NTGF is less sensitive to substrate stiffness compared to STGF; (iii) STGF is caused by higher surface traction compared to that causing NTGF; and (iv) plaques that failed in the STGF mode have higher load bearing capacity than those that failed with NTGF mode.

To question if the pulling angle is the primary factor that determined the failure mode, a series of experimental measurements were conducted. Figure 4*f* shows the frequency of different failure modes that occurred on different substrates. When the pulling angle exceeded 45°, all mussel plaques failed in the NTGF mode regardless of substrate stiffness. The high level of determinacy observed may suggest that the pulling angle was the main contributing factor in this condition. However, when the pulling angle was less than 45°, which was closer to the natural loading scenarios, the frequency of the STGF mode increased from 0.4 to 1 as the substrate stiffness increased to 1.68 MPa. This observed uncertainty may indicate that the failure mode may also be influenced by the stiffness of the substrate under smaller pulling angles. The statistical significance of the substrate stiffness and the pulling angle was confirmed by a two-way ANOVA test using the Tukey mean comparison method. Figure 4*g* shows that substrate stiffness was statistically significant to T_{max} under small pulling angle (< 45°) but statistically insignificant under large pulling angle (> 45°). This finding suggested a synergistic effect of the pulling angle and substrate stiffness on T_{max} under a small pulling angle (< 45°).

(b) Responses of a mussel plaque under directional tensions

The two distinct failure modes, i.e. NTGF and STGF, are associated with two different types of deformation patterns of mussel plaques. Figure 5*a,b* shows the FE predicted and measured functional relations between applied surface traction **T** and the plaque strain ε_p for selected loading directions for the mussel plaques detached from the stiff and the soft PDMS substrates, respectively. The FE predictions agree well with the experimental measurement. The failure mode for each scenario has been highlighted in these figures, which suggests that, for both failure modes, the surface traction **T** increased monotonically with plaque strain until the final catastrophic failure occurred. FE predictions and experimental measurements suggest that (i) the plaque detached with the STGF mode exhibited a much smaller value of plaque strain ε_p at failure than those detached with the NTGF mode (figure 5*a*); (ii) an increase in substrate stiffness from 0.57 to 1.68 MPa resulted in a moderate reduction in plaque strain at failure (figure 5*a,b*); and (iii) plaque strain ε_p at failure increased as the pulling angle increased (figure 5*c*) while the total strain (ε_t) experienced an opposite trend (figure 4*a,b*). The plaque strain under 45° tension is in the range of 1.2–1.6, which is consistent with previous strain measurements (1.3–2.2) [48].

To further reveal the deformation mechanism, figure 5*f,g* shows montages of the selected bottom views and side views during the loading history of plaques that failed with STGF (i.e. θ = 15°) and NTGF modes (i.e. θ = 45°), respectively, as indicated in figure 5*a*. To aid in the interpretation of the results, the figures also include schematic side views depicting the debonding processes. In the STGF mode, the mussel plaque exhibited a sudden and catastrophic manner: no interfacial damage was observed until immediate before failure (Point IV). However, in the NTGF mode, the plaque failed in a progressive manner: debonding

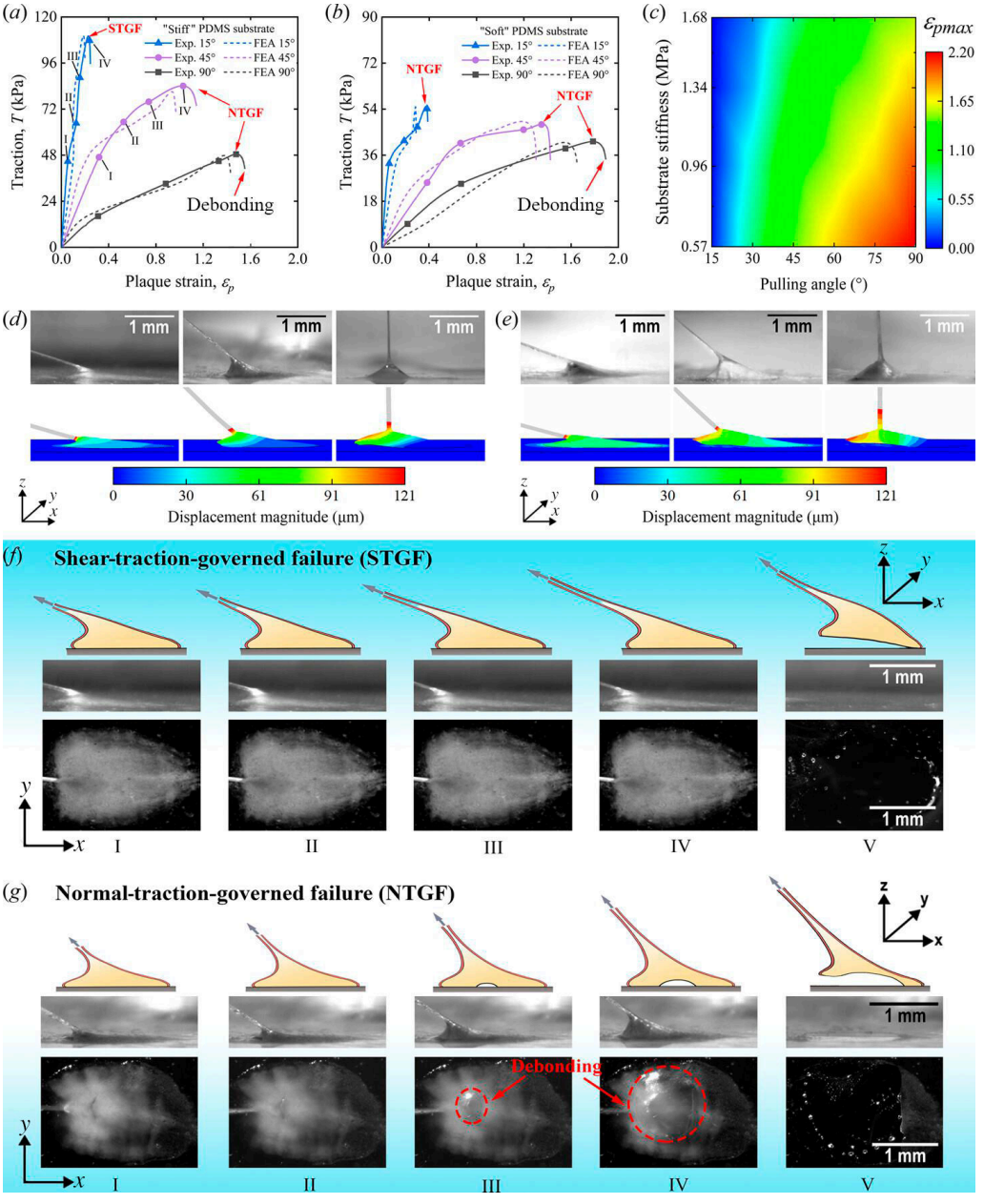

Figure 5. Deformation of mussel plaques under directional tension. (*a*) and (*b*) A comparison of the FE predicted strain of the mussel plaque with experimental measurements at loading stages I to IV, detaching mussel plaques from stiff and soft substrates, respectively. (*c*) The maximum strain of the mussel plaque (ε_{pmax}) in response to different substrate stiffness and pulling angle. ε_{pmax} are the mean values of five individual measurements from the experiments. (*d*) and (*e*) The side view of FE predicted maximum plaque deformation against experimental images, detaching mussel plaques from stiff and soft substrates, respectively. (*f*) and (*g*) Schematic side views in conjunction with time-lapse plaque projections to show the evolution of STGF and NTGF from I to V of (*a*,*b*) respectively.

was initiated underneath the location of the thread (Point II) and propagated rapidly until it was fully deboned from the substrate (Point V). It is noted that, although the NTGF mode exhibits a progressive failure mode at the interface, there is an increase in surface traction **T** over the entire process of debonding (Points I–IV), as shown in figure 5*a*,*b*. This is distinct

from conventional engineering systems, which typically exhibit a noticeable and progressive reduction in load-bearing capacity as they undergo progressive failure.

(c) *In situ* DIC measurement on plaque and substrate interactions

The deformation patterns exhibited by a deformable substrate under a plaque–substrate interaction event can provide clues on how the traction forces are transmitted from a plaque to the underlying substrate, which can further strengthen our understanding of the interaction event. We used two-dimensional *in situ* DIC to measure the in-plane maximum and minimum principal strains, ε_{max} and ε_{min}, on the top surface of the stiff and soft substrates during directional tensile tests. To ensure that the mfps at the interfaces were fully developed, the plaques were brought into contact with the underlying substrates for a period of 48 h prior to tensile tests; FE predictions were also conducted for interpretation and comparison purposes. In accordance with the convention of principal strain [85], a positive value was defined as tension, while a negative value was defined as compression. The arrows in the distribution of ε_{max} and ε_{min} denoted the orientation of the principal planes.

Figure 6 shows montages at selected loading stages, showing the side view of plaque deformation, in-plane principal strains and FE predicted damage variable at the interface (cohesive element) for the plaque that was detached from the stiff substrate under 15° tension and failed under the STGF mode. *In situ* DIC and FE simulation show that the vicinity directly beneath the intersection of the thread and plaque, i.e. the rear portion, experienced compression in both in-plane principal directions. Moving away from the rear portion towards the front portion, the maximum principal strain ε_{max} of the underlying substrate gradually shifted from compression to tension (figure 6*b*), while the minimum principal strain ε_{min} remained in compression (figure 6*c*). The highest tensile strain was observed around the front and side boundaries of the mussel plaque, with principal angles varying from −43.94 to 44.14° with respect to the outward normal of the plaque boundary (figure 6*b*). The FE predictions show a reasonable agreement with the *in situ* DIC measurements. Consistent with experimental observation (figure 5*f*), FE predictions demonstrated that no significant debonding occurred within the interaction prior to failure, and the interface failed suddenly and catastrophically (figure 6*d*). During the loading process, the mussel plaque experienced insignificant deformation (figure 6*a*), and the geometrical sizes and positions of the compression and tension zones (figure 6*b,c*) remained approximately constant owing to the lack of debonding at the interface.

The plaques detached from the soft substrate under 15° tension failed under the NTGF mode (figure 5*g*). During the loading process, the mussel plaque exhibited a noticeable deformation, as shown at point IV of figure 7*a*. In comparison to the stiff substrate, a lower traction (T_{max}) induced by a 15° tension resulted in a relatively larger deformation on the soft substrate. Maximum and minimum strains (ε_{max} and ε_{min}) from I to IV were within the range of −0.073 to 0.111 and −0.116 to 0, respectively. This can be primarily attributed to the lower stiffness of the underlying substrate. Again, the highest in-plane tensile strain in the substrate was observed around the front and side boundaries of the mussel plaque (figure 7*b*), and the substrate around the rear portion experienced compression in both in-plane principal directions (figure 7*b,c*). The interfaces failed in a progressive failure mode, with debonding starting from the rear portion and gradually spreading towards the front portion (figure 7*d*). As a result, the geometric sizes and positions of the compression and tension zones constantly change, with the compression zone expanding and shifting towards the front boundary (figure 7*b*). Plaques under 45° tension, detached from both the soft and stiff substrates, exhibit a similar deformation pattern, as shown in the electronic supplementary material, figures S13 and S14 [57]. Consistent with prior works that detached plaques from glass substrates [48,53], the tensile load carried by the plaque–thread system increased monotonically regardless of the occurrence of NTGF

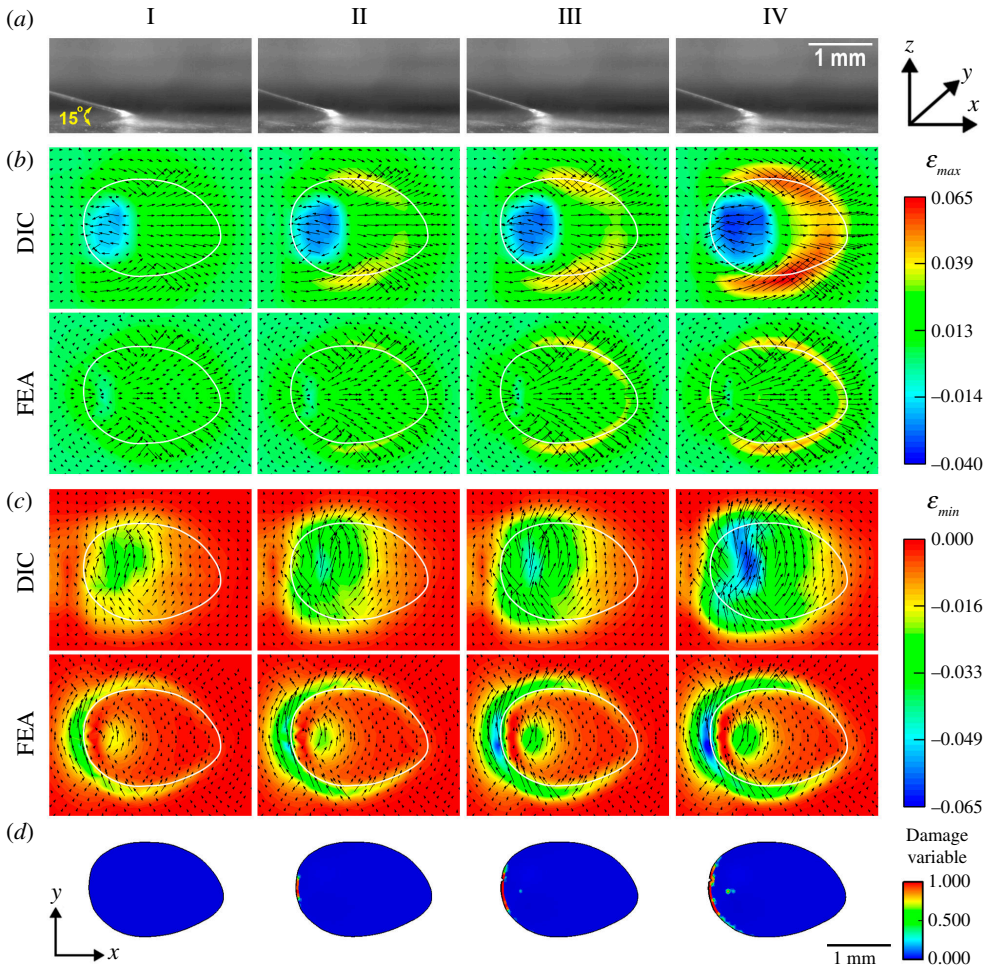

Figure 6. Mussel plaque and substrate interaction on 'hard' substrate under 15° tension. (*a*) The side view of mussel plaque detaching under 15° tension. (*b*) and (*c*) Comparisons of *in situ* DIC measurements and FE predictions showing the evolution of ε_{max} and ε_{min} on 'hard' substrate, respectively. (*d*) The evolution of FE predicted cohesive failure on 'hard' substrate. Note that there is no debonding failure at the interface, and the scalar damage variables are below the threshold of element deletion.

(figure 4*b*). This phenomenon could be attributed to the remarkable ability of deformation redistribution in mussel plaques, progressively increasing and shifting the high in-plane ε_{max} zone towards the front boundary in response to the reduction in adhesion area caused by debonding.

The deformation pattern of the stiff substrate caused by the 90° tension is distinct from those caused by 15° or 45° tensions, as shown in figure 8*b*,*c*. The interfaces failed in a progressive failure mode, with debonding starting from the centre of the rear portion and gradually extending towards the outer edge of the rear portion (figure 8*d*). Both the FE simulation and the *in situ* DIC measurement showed a ring pattern in the distribution of ε_{max} with compression in the interior and tension in the exterior. The scaling varies between −0.024 and 0.017 from region I to IV (see figure 8*b*). Additionally, the distribution of ε_{min}, ranging between −0.027 and 0 from I to IV, exhibits a circle pattern with high in-plane compression in the centre that decreases radially (figure 8*c*). Debonding rapidly developed from III to IV, which caused a reduction of strain intensity at the compression zone (figure 8*d*). The mussel plaque deforms significantly owing to the presence of debonding (figure 8*a*). The substrate around the rear portion is the

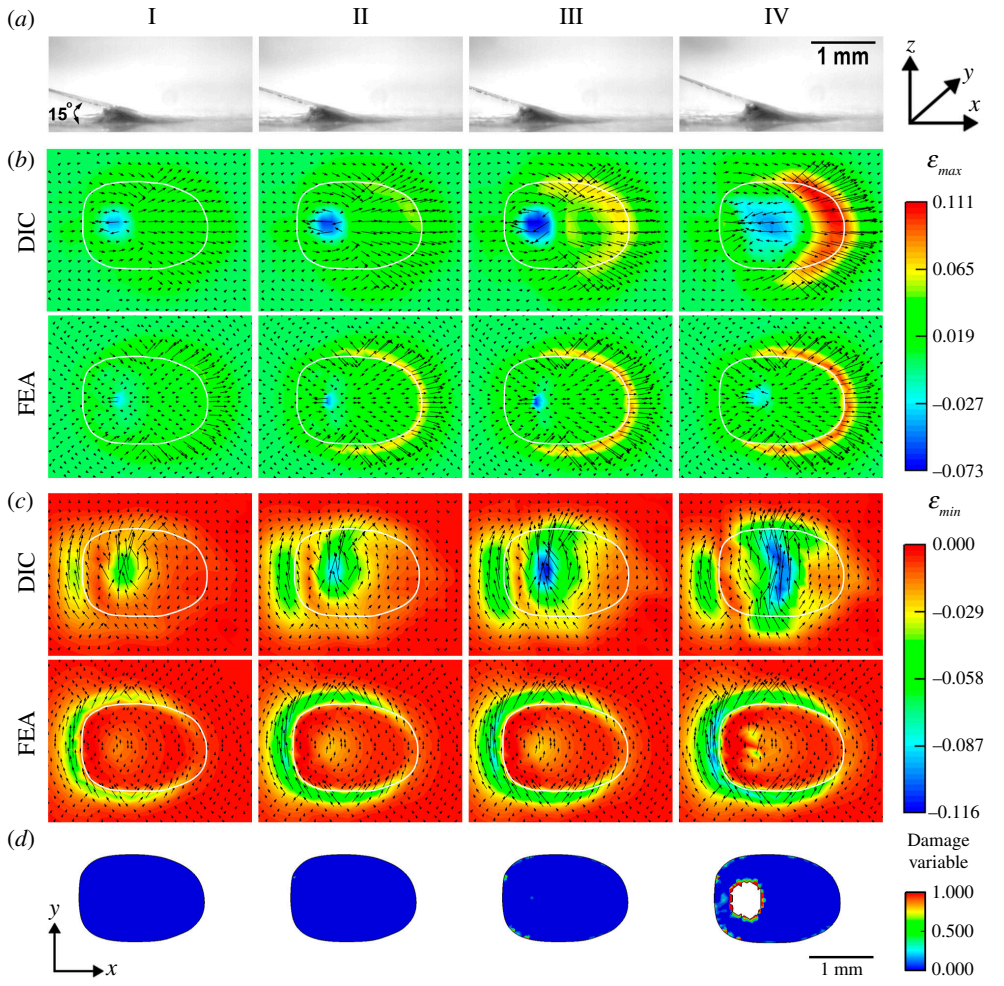

Figure 7. Mussel plaque and substrate interaction on soft substrate under 15° tension. (*a*) The side view of mussel plaque detaching under 15° tension. (*b*) and (*c*) Comparisons of DIC measurements and FE predictions showing the evolution of ε_{max} and ε_{min} on soft substrate, respectively. (*d*) The evolution of FE predicted cohesive failure on a soft substrate. Note that debonding failure occurred at Point IV and the scalar damage variables exceeded the threshold of element deletion.

only area where the in-plane principal strains were detected. The absence of in-plane principal strains in the front portion may suggest that the front portion did not contribute to the in-plane loading bearing. The deformation pattern of the soft substrate under 90° tension is similar to that of the stiff substrate (electronic supplementary material, figure S15 [57]).

4. Discussion

The distinctive adhesive structure of mussel plaques plays a vital role in facilitating robust adhesion on wet substrates, which allows marine mussels to endure the significant forces generated by turbulent tidal currents and predator attacks. In this study, directional tension experiments were performed to investigate the responses of isolated mussel plaques when subjected to selected pulling angles and substrate stiffness. We used a specially designed microscope system integrated with two-dimensional *in situ* DIC to measure the in-plane deformation of a deformable substrate when it interacted with a mussel plaque while being subjected to directional tension. To replicate real working conditions, directional tension

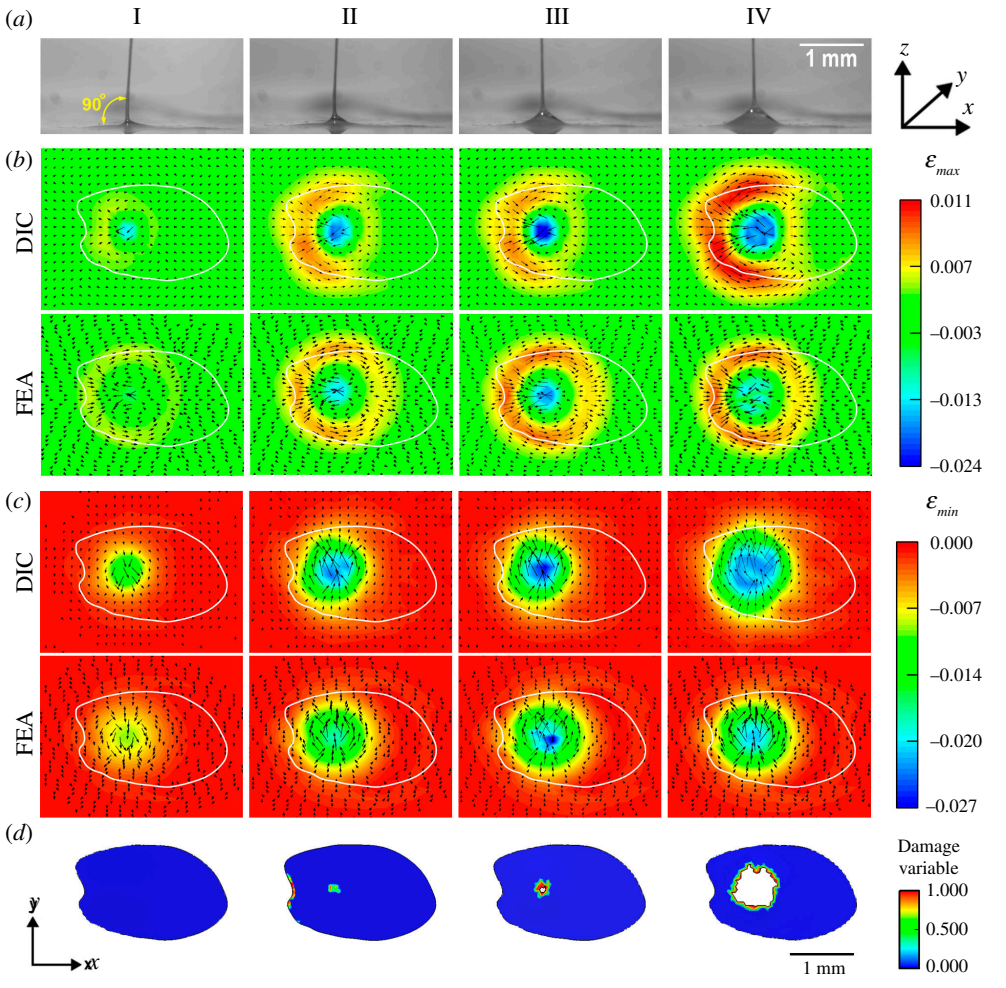

Figure 8. Mussel plaque and substrate interaction in response to 90° tension. (*a*) The side view of mussel plaque detaching from the substrate under 90° tension. (*b*) and (*c*) Comparisons of DIC measurements and FE predictions showing the evolution of ε_{max} and ε_{min} under 90° tension, respectively. (*d*) The evolution of FE predicted cohesive failure under 90° tension. Note that stiff substrates are used here to compare FE simulation and *in situ* DIC measurement. The deformation pattern on the soft PDMS substrate was given in electronic supplementary material, figure S15 [57].

experiments were conducted under wet conditions, i.e. both the plaque and the substrate were fully immersed in seawater during experiments. This contrasts with previous experiments on directional tension, which were predominantly carried out in either moist or dry environments [30,48,53]. In line with previous studies [28,48], NTGF was identified as a common mode of failure observed when mussel plaques were removed from the substrates at pulling angles greater than 45°. Interestingly, a novel mode of failure, namely, STGF, was discovered when mussel plaques were detached from stiff substrates at a lower pulling angle (e.g. 15°), closely aligned with the natural angle of the plaque. Our study found that the plaque–thread system failed in the STGF mode exhibits higher surface traction (figure 4*c*) and less plaque deformation than the NTGF mode (figure 5*a–c*), which demonstrates the mechanical advantages of anchoring to stiff substrates at a smaller pulling angle. Furthermore, the STGF mode demonstrates an abrupt and catastrophic failure mode, whereas the NTGF mode exhibits a gradual and progressive failure mode. Significantly, the findings of this study differ from previous research,

as no experimental evidence of interior and exterior cohesive failures was observed in mussel plaques [48]. These discrepancies may be attributed to variations in mussel species (*M. edulis* or *Mytilus californianus*), testing environments (water immersed, moist or dry), substrate conditions (surface functional groups, roughness and hydrophilicity). Furthermore, the previous investigation reported that pulling angles are the primary factor affecting the failure modes of plaque detachment [48]; however, the present study emphasizes the significance of substrate stiffness and reveals a synergistic effect of the pulling angle and substrate stiffness on plaque detachment.

The two-dimensional *in situ* DIC measurements revealed the detailed in-plane deformation pattern of the underlying deformable substrate, which could provide insight into how in-plane traction forces were transmitted from the mussel plaque to the underlying substrate. The experimental measurements were compared with the numerical results obtained by full-scale, detailed FE simulations, which showed good correlations. Our results suggested that (i) plaque contraction caused by directional tension could introduce in-plane tension and compression in the substrate around the front and rear portion of the plaque, respectively; (ii) prior to failure, interfacial damage/debonding was observed around the compression zone in the case of the NTGF mode, which caused a reduction in strain intensity in the compression zone. On the other hand, no interfacial damage/debonding was detected for the STGF mode; and (iii) when the pulling angle reaches 90°, a notable shift occurs in the tension zone towards the rear section of the plaque. This shift was manifest as a distinctive 'ring' pattern characterized by compression in the interior and tension in the exterior. This observation suggested that the front portion of the plaque does not contribute significantly to bearing the in-plane loading. It is important to note that obvious strain concentrations were found near plaque edges in the FE simulations. This discrepancy was mainly caused by minor geometry variations between the FE models and the real plaques. In the FE model, the boundary of mussel plaques was clearly defined (electronic supplementary material, figure S16*a* [57]), which causes a sudden change in stiffness from plaque to substrate. Conversely, real mussel plaques exhibited a blurred boundary along the edges (electronic supplementary material, figure S16*b* [57]), resulting in a gradual transition in stiffness from plaque to substrate. To address this discrepancy, a potential solution is the reconstruction of the FE model using computed tomography (CT) scan data derived from a real mussel plaque. Consistent with previous works on the debonding gecko- and mussel-inspired structures [86–88], the scalloped edges of the adhesive structure were critical to managing strain concentrations. Our experimental measurements further confirmed that a blurred and scalloped edge of the mussel plaque performs better than clear edges in reducing strain concentration by inducing a larger deformed area on the substrate.

Further studies should focus on the advancement of the current FE model and experimental methods. First, in the present study, the mechanical properties of the cohesive layer were determined by calibrating the FE simulated traction–strain curves with DIC measurements. In reality, these adhesive properties (table 1) may not be unique or evenly distributed at the plaque/substrate interface, as they could potentially be influenced by protein concentration, maturity and distribution. Thus, further study could focus on establishing the correlations between protein conditions and adhesive properties using AFM. Second, although equivalent solids can accurately capture the global responses of the porous core under tension, this approach cannot model the deformation of pore walls and the interaction between coarse and fine pores. Therefore, future FE simulation is recommended to construct a real porous structure based on nano-CT scanning or confocal laser scanning. Third, since substrate deformations are thickness dependent, future investigations are recommended to quantify the effects of substrate thickness on displacement and strain intensities at plaque/substrate interface. Furthermore, the proposed microscope system successfully captured the average traction and two-dimensional deformation at the substrates. This system could be further extended to achieve three-dimensional full-field traction force measurement and study plaque/substrate interaction events.

The insights obtained from the interaction between the plaque and the substrate offer valuable mechanical and structural knowledge, opening up various new avenues for research. Specifically, this study provides inspiration for developing general strategies or design principles for interfacial adhesive structures that can effectively join materials with distinct stiffness. Additionally, our study sheds light on the potential development of wet adhesives for biomedical applications, including internal wound-healing patches and adhesive coatings for medical implants.

Ethics. Experiments using marine mussels funded by the Leverhulme Trust comply with the Animals (Scientific Procedures) Act 1986 (ASPA).

Data accessibility. The data are provided in electronic supplementary material [57].

Declaration of AI use. We have not used AI-assisted technologies in creating this article.

Authors' contributions. Y.P.: conceptualization, data curation, formal analysis, investigation, methodology, software, validation, visualization, writing—original draft, writing—review and editing; W.S.: supervision, writing—review and editing; T.L.: conceptualization, data curation, funding acquisition, investigation, methodology, project administration, supervision, validation, writing—original draft, writing—review and editing.

All authors gave final approval for publication and agreed to be held accountable for the work performed therein.

Conflict of interest declaration. We declare we have no competing interests.

Funding. This work was funded by the Leverhulme Trust Research Grant Scheme, UK (No. RPG-2020-235).

Acknowledgements. The authors acknowledge the use of the instruments and scientific and technical assistance at NanoVision Centre, Queen Mary University London. We acknowledge Professor Robert M. McMeeking from the University of California, Santa Barbara for early discussions to initiate this research. We also acknowledge all valuable comments received from our reviewers.

References

1. Fan H, Gong JP. 2021 Bioinspired underwater adhesives. *Adv. Mater.* **33**, e2102983. (doi:10.1002/adma.202102983)
2. Stewart RJ, Ransom TC, Hlady V. 2011 Natural underwater adhesives. *J. Polym. Sci. B. Polym. Phys.* **49**, 757–771. (doi:10.1002/polb.22256)
3. Chen Y, Meng J, Gu Z, Wan X, Jiang L, Wang S. 2020 Bioinspired multiscale wet adhesive surfaces: structures and controlled adhesion. *Adv. Funct. Mater.* **30**, 1905287. (doi:10.1002/adfm.201905287)
4. Lyu Y, Pang Y, Liu T, Sun W. 2024 Determining hyperelastic properties of the constituents of the mussel byssus system. *Soft Matter* **20**, 2442–2454. (doi:10.1039/D3SM01677C)
5. Heydari S, Johnson A, Ellers O, McHenry MJ, Kanso E. 2020 Sea star inspired crawling and bouncing. *J. R. Soc. Interface* **17**, 20190700. (doi:10.1098/rsif.2019.0700)
6. Karlsson Green K, Kovalev A, Svensson EI, Gorb SN. 2013 Male clasping ability, female polymorphism and sexual conflict: fine-scale elytral morphology as a sexually antagonistic adaptation in female diving beetles. *J. R. Soc. Interface* **10**, 20130409. (doi:10.1098/rsif.2013.0409)
7. Tramacere F, Beccai L, Kuba M, Gozzi A, Bifone A, Mazzolai B. 2013 The morphology and adhesion mechanism of octopus vulgaris suckers. *PLoS One* **8**, e65074. (doi:10.1371/journal.pone.0065074)
8. Meng F, Liu Q, Wang X, Tan D, Xue L, Barnes WJP. 2019 Tree frog adhesion biomimetics: opportunities for the development of new, smart adhesives that adhere under wet conditions. *Phil. Trans. R. Soc. A* **377**, 20190131. (doi:10.1098/rsta.2019.0131)
9. Ditsche P, Summers A. 2019 Learning from Northern clingfish (Gobiesox maeandricus): bioinspired suction cups attach to rough surfaces. *Philos. Trans. R. Soc. Lond., B, Biol. Sci.* **374**, 20190204. (doi:10.1098/rstb.2019.0204)
10. Lin AYM, Brunner R, Chen PY, Talke FE, Meyers MA. 2009 Underwater adhesion of abalone: the role of van der Waals and capillary forces. *Acta Materialia* **57**, 4178–4185. (doi:10.1016/j.actamat.2009.05.015)

11. Labonte D, Federle W. 2015 Scaling and biomechanics of surface attachment in climbing animals. *Philos. Trans. R. Soc. Lond. B. Biol. Sci.* **370**, 20140027. (doi:10.1098/rstb.2014.0027)
12. Slater DM, Vogel MJ, Macner AM, Steen PH. 2014 Beetle-inspired adhesion by capillary-bridge arrays: pull-off detachment. *J. Adhes. Sci. Technol.* **28**, 273–289. (doi:10.1080/01694243.2012.705472)
13. Yang J, Bai R, Chen B, Suo Z. 2020 Hydrogel adhesion: a supramolecular synergy of chemistry, topology, and mechanics. *Adv. Funct. Mater.* **30**, 1901693. (doi:10.1002/adfm.201901693)
14. Park HH, Seong M, Sun K, Ko H, Kim SM, Jeong HE. 2017 Flexible and shape-reconfigurable hydrogel interlocking adhesives for high adhesion in wet environments based on anisotropic swelling of hydrogel microstructures. *ACS Macro Lett.* **6**, 1325–1330. (doi:10.1021/acsmacrolett.7b00829)
15. Amador GJ, Endlein T, Sitti M. 2017 Soiled adhesive pads shear clean by slipping: a robust self-cleaning mechanism in climbing beetles. *J. R. Soc. Interface* **14**, 20170134. (doi:10.1098/rsif.2017.0134)
16. Lee SH, Song HW, Kang BS, Kwak MK. 2019 Remora-inspired reversible adhesive for underwater applications. *ACS Appl. Mater. Interfaces* **11**, 47571–47576. (doi:10.1021/acsami.9b16350)
17. Chuang YC, Chang HK, Liu GL, Chen PY. 2017 Climbing upstream: multi-scale structural characterization and underwater adhesion of the pulin river loach (*Sinogastromyzon puliensis*). *J. Mech. Behav. Biomed. Mater.* **73**, 76–85, (doi:10.1016/j.jmbbm.2017.01.029)
18. Ditsche-Kuru P, Koop JHE, Gorb SN. 2010 Underwater attachment in current: the role of setose attachment structures on the gills of the mayfly larvae *Epeorus assimilis* (Ephemeroptera, Heptageniidae). *J. Exp. Biol.* **213**, 1950–1959. (doi:10.1242/jeb.037218)
19. Kavanagh CJ, Schultz MP, Swain GW, Stein J, Truby K, Wood CD. 2001 Variation in adhesion strength of *Balanus eburneus, Crassostrea virginica* and *Hydroides dianthus* to fouling-release coatings . *Biofouling* **17**, 155–167. (doi:10.1080/08927010109378474)
20. Rittschof D, Orihuela B, Stafslien S, Daniels J, Christianson D, Chisholm B, Holm E. 2008 Barnacle reattachment: a tool for studying barnacle adhesion. *Biofouling* **24**, 1–9. (doi:10.1080/08927010701784920)
21. Holm ER et al. 2006 Interspecific variation in patterns of adhesion of marine fouling to silicone surfaces. *Biofouling* **22**, 233–243. (doi:10.1080/08927010600826129)
22. Lin Q, Gourdon D, Sun C, Holten-Andersen N, Anderson TH, Waite JH, Israelachvili JN. 2007 Adhesion mechanisms of the mussel foot proteins mfp-1 and mfp-3. *Proc. Natl. Acad. Sci. USA.* **104**, 3782–3786. (doi:10.1073/pnas.0607852104)
23. George MN, Pedigo B, Carrington E. 2018 Hypoxia weakens mussel attachment by interrupting DOPA cross-linking during adhesive plaque curing. *J. R. Soc. Interface* **15**, 20180489. (doi:10.1098/rsif.2018.0489)
24. Priemel T, Palia G, Förste F, Jehle F, Sviben S, Mantouvalou I, Zaslansky P, Bertinetti L, Harrington MJ. 2021 Microfluidic-like fabrication of metal ion-cured bioadhesives by mussels. *Science* **374**, 206–211. (doi:10.1126/science.abi9702)
25. Silverman HG, Roberto FF. 2007 Understanding marine mussel adhesion. *Mar. Biotechnol. (NY)* **9**, 661–681. (doi:10.1007/s10126-007-9053-x)
26. Yu J et al. 2013 Adaptive hydrophobic and hydrophilic interactions of mussel foot proteins with organic thin films. *Proc. Natl. Acad. Sci. U. S. A.* **110**, 15680–15685. (doi:10.1073/pnas.1315015110)
27. Lee H, Scherer NF, Messersmith PB. 2006 Single-molecule mechanics of mussel adhesion. *Proc. Natl. Acad. Sci. USA.* **103**, 12999–13003. (doi:10.1073/pnas.0605552103)
28. Waite JH. 2017 Mussel adhesion - essential footwork. *J. Exp. Biol.* **220**, 517–530. (doi:10.1242/jeb.134056)
29. Filippidi E, DeMartini DG, Malo de Molina P, Danner EW, Kim J, Helgeson ME, Waite JH, Valentine MT. 2015 The microscopic network structure of mussel (Mytilus) adhesive plaques. *J. R. Soc. Interface* **12**, 20150827. (doi:10.1098/rsif.2015.0827)
30. Qin Z, Buehler MJ. 2013 Impact tolerance in mussel thread networks by heterogeneous material distribution. *Nat. Commun.* **4**, 1–8. (doi:10.1038/ncomms3187)

31. Valois E, Hoffman C, Demartini DG, Waite JH. 2019 The thiol-rich interlayer in the shell/core architecture of mussel byssal threads. *Langmuir* **35**, 15985–15991. (doi:10.1021/acs.langmuir.9b01844)
32. Jehle F, Macías-Sánchez E, Sviben S, Fratzl P, Bertinetti L, Harrington MJ. 2020 Hierarchically-structured metalloprotein composite coatings biofabricated from co-existing condensed liquid phases. *Nat. Commun.* **11**, 862. (doi:10.1038/s41467-020-14709-y)
33. Harrington MJ, Masic A, Holten-Andersen N, Waite JH, Fratzl P. 2010 Iron-clad fibers: a metal-based biological strategy for hard flexible coatings. *Science* **328**, 216–220. (doi:10.1126/science.1181044)
34. Bernstein JH, Filippidi E, Herbert Waite J, Valentine MT. 2020 Effects of sea water pH on marine mussel plaque maturation. *Soft Matter* **16**, 9339–9346. (doi:10.1039/d0sm01237h)
35. Chisca S, Musteata VE, Sougrat R, Behzad AR, Nunes SP. 2018 Artificial 3D hierarchical and isotropic porous polymeric materials. *Sci. Adv.* **4**, eaat0713. (doi:10.1126/sciadv.aat0713)
36. Yang T, Jia Z, Wu Z, Chen H, Deng Z, Chen L, Zhu Y, Li L. 2022 High strength and damage-tolerance in echinoderm stereom as a natural bicontinuous ceramic cellular solid. *Nat. Commun.* **13**, 1–12. (doi:10.1038/s41467-022-33712-z)
37. Shi S, Li Y, Ngo-Dinh BN, Markmann J, Weissmüller J. 2021 Scaling behavior of stiffness and strength of hierarchical network nanomaterials. *Science* **371**, 1026–1033. (doi:10.1126/science.abd9391)
38. Pham MS, Liu C, Todd I, Lertthanasarn J. 2019 Damage-tolerant architected materials inspired by crystal microstructure. *Nature* **565**, 305–311. (doi:10.1038/s41586-018-0850-3)
39. Liu C, Lertthanasarn J, Pham MS. 2021 The origin of the boundary strengthening in polycrystal-inspired architected materials. *Nat. Commun.* **12**, 4600, (doi:10.1038/s41467-021-24886-z)
40. Shaikeea AJD, Cui H, O'Masta M, Zheng XR, Deshpande VS. 2022 The toughness of mechanical metamaterials. *Nat. Mater.* **21**, 297–304. (doi:10.1038/s41563-021-01182-1)
41. Bhuwal AS, Pang Y, Ashcroft I, Sun W, Liu T. 2023 Discovery of quasi-disordered truss metamaterials inspired by natural cellular materials. *J. Mech. Phys. Solids* **175**, 105294. (doi:10.1016/j.jmps.2023.105294)
42. Yang T, Chen H, Jia Z, Deng Z, Chen L, Peterman EM, Weaver JC, Li L. 2022 A damage-tolerant, dual-scale, single-crystalline microlattice in the knobby starfish, *Protoreaster nodosus* *Science* **375**, 647–652. (doi:10.1126/science.abj9472)
43. Bhuwal AS, Pang Y, Maskery I, Ashcroft I, Sun W, Liu T. Creep Characterization of Inconel 718 Lattice Metamaterials Manufactured by Laser Powder Bed Fusion. *Adv. Eng. Mater.* (doi:10.1002/adem.202300643)
44. Monnier CA, DeMartini DG, Waite JH. 2018 Intertidal exposure favors the soft-studded armor of adaptive mussel coatings. *Nat. Commun.* **9**, 3424. (doi:10.1038/s41467-018-05952-5)
45. Aldred N, Wills T, Williams DN, Clare AS. 2007 Tensile and dynamic mechanical analysis of the distal portion of mussel (Mytilus edulis) byssal threads. *J. R. Soc. Interface* **4**, 1159–1167. (doi:10.1098/rsif.2007.1026)
46. Xu Q et al. 2019 Metal coordination-mediated functional grading and self-healing in mussel byssus cuticle. *Adv. Sci.* **6**, 1902043. (doi:10.1002/advs.201902043)
47. Renner-Rao M, Jehle F, Priemel T, Duthoo E, Fratzl P, Bertinetti L, Harrington MJ. 2022 Mussels fabricate porous glues via multiphase liquid-liquid phase separation of multiprotein condensates. *ACS Nano* **16**, 20877–20890. (doi:10.1021/acsnano.2c08410)
48. Desmond KW, Zacchia NA, Waite JH, Valentine MT. 2015 Dynamics of mussel plaque detachment. *Soft Matter* **11**, 6832–6839. (doi:10.1039/c5sm01072a)
49. Kwon Y, Bernstein JH, Cohen N, Valentine MT. 2021 On-demand manufacturing capabilities of mussels enable robust adhesion to geometrically complex surfaces. *ACS Biomater. Sci. Eng.* **7**, 5099–5106. (doi:10.1021/acsbiomaterials.1c00845)
50. Amini S et al. 2017 Preventing mussel adhesion using lubricant-infused materials. *Science* **357**, 668–673. (doi:10.1126/science.aai8977)
51. Kang T et al. 2016 Mussel-inspired anchoring of polymer loops that provide superior surface lubrication and antifouling properties. *ACS Nano* **10**, 930–937. (doi:10.1021/acsnano.5b06066)

52. Carrington E, Gosline JM. 2004 *mechanical design of Mussel Byssus: load cycle and strain rate Dependence*. Amal. Malacol. Bull, pp. 135–142. See https://digitalcommons.uri.edu/bio_facpubs/188/.
53. Wilhelm MH, Filippidi E, Waite JH, Valentine MT. 2017 Influence of multi-cycle loading on the structure and mechanics of marine mussel plaques. *Soft Matter* **13**, 7381–7388. (doi:10.1039/c7sm01299c)
54. Bertoldi K, Boyce MC. 2007 Mechanics of the hysteretic large strain behavior of mussel byssus threads. *J. Mater. Sci.* **42**, 8943–8956. (doi:10.1007/s10853-007-1649-z)
55. Choi J, Lee S, Ohkawa K, Hwang DS. 2021 Counterplotting the mechanosensing-based fouling mechanism of mussels against fouling. *ACS Nano* **15**, 18566–18579. (doi:10.1021/acsnano.1c09097)
56. Ghareeb A, Elbanna A. 2018 On the role of the plaque porous structure in mussel adhesion: implications for adhesion control using bulk patterning. *J. Appl. Mech.* **85**, 121003. (doi:10.1115/1.4041223)
57. Pang Y, Sun W, Liu T. 2024 Data from: Quasi-static responses of marine mussel plaques detached from deformable wet substrates under directional tensions. *FigShare* (doi:10.6084/m9.figshare.c.7204009)
58. Nordestgaard BG, Rostgaard J. 1985 Critical-point drying versus freeze drying for scanning electron microscopy: a quantitative and qualitative study on isolated hepatocytes. *J. Microsc.* **137**, 189–207. (doi:10.1111/j.1365-2818.1985.tb02577.x)
59. Bray DF, Bagu J, Koegler P. 1993 Comparison of hexamethyldisilazane (HMDS), Peldri II, and critical-point drying methods for scanning electron microscopy of biological specimens. *Microsc. Res. Tech.* **26**, 489–495. (doi:10.1002/jemt.1070260603)
60. ANSI webstore. 2016 ASTM D412-16. Standard test methods for vulcanized rubber and thermoplastic elastomers-tension. ASTM International, West Conshohocken.
61. Liu M, Sun J, Sun Y, Bock C, Chen Q. 2009 Thickness-dependent mechanical properties of polydimethylsiloxane membranes. *J. Micromech. Microeng.* **19**, 035028. (doi:10.1088/0960-1317/19/3/035028)
62. Stark AY, Badge I, Wucinich NA, Sullivan TW, Niewiarowski PH, Dhinojwala A. 2013 Surface wettability plays a significant role in gecko adhesion underwater. *Proc. Natl. Acad. Sci. U. S. A.* **110**, 6340–6345. (doi:10.1073/pnas.1219317110)
63. Turner D. 2015 Digital image correlation engine (dice) reference manual. Sandia report, Sand2015-10606 O.
64. Moon Jeong S, Song S, Lee SK, Choi B. 2013 Mechanically driven light-generator with high durability. *Appl. Phys. Lett.* **102**, 051110. (doi:10.1063/1.4791689)
65. Park HJ et al. 2019 Self-powered motion-driven triboelectric electroluminescence textile system. *ACS Appl. Mater. Interfaces* **11**, 5200–5207. (doi:10.1021/acsami.8b16023)
66. Reu P. 2014 All about speckles: speckle size measurement. *Exp. Techniques* **38**, 1–2. (doi:10.1111/ext.12110)
67. Reu P. 2015 All about speckles: contrast. *Exp. Techniques* **39**, 1–2. (doi:10.1111/ext.12126)
68. Schreier H, Orteu JJ, Sutton MA. 2009 Image correlation for shape, motion and deformation measurements: basic concepts, theory and applications. Boston, MA: Springer Science & Business Media. (doi:%2010.1007/978-0-387-78747-3)
69. Reu P. 2015 All about speckles: speckle density. *Exp. Tech.* **39**, 1–2. (doi:10.1111/ext.12161)
70. Pang Y, Chen BK, Yu SF, Lingamanaik SN. 2020 Enhanced laser speckle optical sensor for in situ strain sensing and structural health monitoring. *Opt. Lett.* **45**, 2331–2334. (doi:10.1364/OL.391582)
71. Su Y, Gao Z, Fang Z, Liu Y, Wang Y, Zhang Q, Wu S. 2019 Theoretical analysis on performance of digital speckle pattern: uniqueness, accuracy, precision, and spatial resolution. *Opt. Express* **27**, 22439–22474. (doi:10.1364/OE.27.022439)
72. Pang Y, Chen BK, Liu W, Yu SF, Lingamanaik SN. 2020 Development of a non-contact and non-destructive laser speckle imaging system for remote sensing of anisotropic deformation around fastener holes. *NDT & E Int.* **111**, 102219. (doi:10.1016/j.ndteint.2020.102219)
73. Ogden RW. 1972 Large deformation isotropic elasticity–on the correlation of theory and experiment for incompressible rubberlike solids. *Proc. R. Soc. Lond. A. Math. Phys. Sci* **326**, 565–584. (doi:10.1098/rspa.1972.0026)

74. Gockowski LF, Dolinski ND, Chavez R, Cohen N, Eisenreich F, Hecht S, McMeeking RM, Hawker CJ, Valentine MT. 2020 Engineering crack tortuosity in printed polymer–polymer composites through ordered pores. *Mater. Horiz.* **7**, 1854–1860. (doi:10.1039/D0MH00331J)
75. Drach B, Tsukrov I, Trofimov A. 2016 Comparison of full field and single pore approaches to homogenization of linearly elastic materials with pores of regular and irregular shapes. *Int. J. Solids Struct* **96**, 48–63. (doi:10.1016/j.ijsolstr.2016.06.023)
76. Cao S, Liu T, Jones A, Tizani W. 2019 Particle reinforced thermoplastic foams under quasi-static compression. *Mech. Mater* **136**, 103081. (doi:10.1016/j.mechmat.2019.103081)
77. Pritchard RH, Lava P, Debruyne D, Terentjev EM. 2013 Precise determination of the Poisson ratio in soft materials with 2D digital image correlation. *Soft Matter* **9**, 6037. (doi:10.1039/c3sm50901j)
78. Valois E, Mirshafian R, Waite JH. 2020 Phase-dependent redox insulation in mussel adhesion. *Sci. Adv.* **6**, eaaz6486. (doi:10.1126/sciadv.aaz6486)
79. Camanho PP, Dávila CG. 2002 *mixed-mode Decohesion finite elements for the simulation of Delamination in composite materials. NASA/TM-2002–211737*. pp. 1–37. See https://ntrs.nasa.gov/citations/20020053651.
80. Harrington MJ, Jehle F, Priemel T. 2018 Mussel byssus structure-function and fabrication as inspiration for biotechnological production of advanced materials. *Biotechnol. J.* **13**, 1800133, (doi:10.1002/biot.201800133)
81. Smeathers JE, Vincent JFV. 1979 Mechanical properties of mussel byssus threads. *J. Molluscan Stud.* **45**, 219–230. (doi:10.1093/oxfordjournals.mollus.a065497)
82. Peng Z, Wang C, Chen L, Chen S. 2014 Peeling behavior of a viscoelastic thin-film on a rigid substrate. *Int. J. Solids Struct.* **51**, 4596–4603. (doi:10.1016/j.ijsolstr.2014.10.011)
83. Shen CS, Wang HF, Du CL. 2022 Peeling of a film from a flexible cantilever substrate. *Mech. Res. Commun.* **119**, 103833. (doi:10.1016/j.mechrescom.2021.103833)
84. Liprandi D, Bosia F, Pugno NM. 2020 A theoretical-numerical model for the peeling of elastic membranes. *J. Mech. Phys. Solids* **136**, 103733. (doi:10.1016/j.jmps.2019.103733)
85. Goodno BJ, Gere JM. 2020 Analysis of stress and strain. In *Mechanics of materials*, pp. 384–393, 9th edn. Cengage Learning.
86. Kamperman M, Kroner E, del Campo A, McMeeking RM, Arzt E. 2010 Functional Adhesive Surfaces with "Gecko" Effect: The Concept of Contact Splitting. *Adv. Eng. Mater.* **12**, 335–348. (doi:10.1002/adem.201000104)
87. Balijepalli RG, Fischer SCL, Hensel R, McMeeking RM, Arzt E. 2017 Numerical study of adhesion enhancement by composite fibrils with soft tip layers. *J. Mech. Phys. Solids* **99**, 357–378. (doi:10.1016/j.jmps.2016.11.017)
88. Paretkar D, Kamperman M, Martina D, Zhao J, Creton C, Lindner A, Jagota A, McMeeking R, Arzt E. 2013 Preload-responsive adhesion: effects of aspect ratio, tip shape and alignment. *J. R. Soc. Interface* **10**, 20130171, (doi:10.1098/rsif.2013.0171)